https://doi.org/10.5194/essd-2026-244
Preprint. Discussion started: 22 June 2026

A multi-scenario proximal hyperspectral dataset of clay-type lithium deposits from China with mineral abundances and geochemistry

Qunjia Zhang[1], Lei Liu[1], Jiacheng Mei[1]

[1]Key Laboratory of Western China's Mineral Resources and Geological Engineering, Ministry of Education, School of Earth Science and Resources, Chang'an University, Xi'an 710054, China

Correspondence to: Lei Liu (liul@chd.edu.cn)

Abstract. Proximal hyperspectral imaging has been widely used in material analysis, mineral mapping, and related geological studies. However, most publicly available datasets are limited to a single observation scenario and commonly lack corresponding mineralogical and geochemical constraints, which restricts quantitative analysis, cross-scenario comparison, and objective method evaluation. To meet this need, this study presents a multi-scenario proximal shortwave infrared imaging hyperspectral dataset for geological samples collected from typical clay-type lithium deposits hosted in carbonate successions in China, systematically covering four complementary observation scenarios, including powder, drill core, hand specimen, and in-situ outcrop. The data were acquired using a HySpex imaging spectrometer covering 960–2500 nm. In addition to the hyperspectral imagery, the dataset integrates mineralogical information, geochemical information, sampling annotations, reference panel spectra, geographic locations, and related metadata, thereby establishing a unified framework linking spectral observations, sample composition, and spatial context. For the controlled indoor scenarios, the dataset provides reflectance data, whereas for the field in-situ scenario it provides radiometrically corrected imagery together with reference panel spectra and example products for data use. The dataset is organized in standard and widely used formats. By covering multiple observation scenarios under the same geological setting and hyperspectral sensor system, and by providing mineralogical and geochemical reference information, it can support model development, domain-shift analysis, and studies linking proximal observations with multi-platform mineral mapping and spectral analysis. The dataset is publicly available on Zenodo at https://doi.org/10.5281/zenodo.19142250 (Zhang et al., 2026a).

1 Introduction

Hyperspectral imaging can acquire continuous spectral and spatial information simultaneously across scales ranging from metres (airborne and spaceborne observation) to millimetres (proximal observation), providing a reliable means for high-resolution and non-destructive analysis of material surfaces (Goetz et al., 1985; Hajaj et al., 2024). The recorded reflectance spectra are functions of the chemical and physical properties of the target material, which interact differently with incident radiation at the molecular and atomic levels (Clark, 2004; Hunt, 1977). As a result, imaging hyperspectral data have been widely applied in resource exploration for detailed drill-core logging, characterization of mineralization zonation, ore sorting, and related geoscientific analyses (Booysen et al., 2022; Corrado et al., 2025; Windrim et al., 2023; Zhang et al., 2026b). However, compared with the rapid development of methods and applications, publicly hyperspectral observation datasets remain relatively limited, particularly imaging hyperspectral datasets that combine high-spatial-resolution observations with corresponding mineralogical and geochemical information. This limitation constrains model development, method validation, and objective evaluation to some extent (Borsoi et al., 2021; Cavalli, 2023; Rasti et al., 2024; Zou et al., 2025).

Publicly available geological hyperspectral data resources have long provided an important foundation for both applied research and algorithm development. A representative example is the classic AVIRIS Cuprite scene in Nevada, for which the imagery and derived mineral maps have been widely used as benchmark data for mineral identification, spectral matching, and endmember extraction, and have played an important role in advancing imaging spectroscopy research and applications (Clark et al., 2003; Swayze et al., 2014; Van Der Meer et al., 2012). At the same time, public spectral libraries such as USGS, ECOSTRESS, and other related resources provide large numbers of reference spectra acquired under laboratory or field conditions, and serve as a general basis for spectral interpretation, spectral matching, and material identification (Baldridge et al., 2009; Cardoso-Fernandes et al., 2023; Clark et al., 2007; Kokaly et al., 2017; Meerdink et al., 2019). These resources are highly valuable in terms of standardized conditions, material coverage, and spectral reference. However, they are commonly dominated by powdered natural or synthetic materials, or a number of standard samples, and most are based primarily on point spectroscopy rather than imaging hyperspectral observations.

In recent years, with advances in sensor technology and increasing demands for analytical accuracy and spatial resolution, proximal hyperspectral imaging has been more widely applied in geological studies (Corrado et al., 2025; Lorenz et al., 2021; Scafutto et al., 2016; Windrim et al., 2023). Some high-quality proximal datasets have also become publicly available. For example, the National Virtual Core Library (NVCL) in Australia has accumulated large volumes of visible near infrared core spectra and imagery, providing important support for mineral identification and digital core analysis (Huntington, 2016; Schodlok et al., 2016). Sample-scale hyperspectral datasets such as HIDSAG further emphasize multimethod characterization and suitability for machine learning applications (Ehrenfeld et al., 2023; Koerting et al., 2021). In addition, independently released mineralogical datasets, such as mineral abundance results derived from XRD and Rietveld refinement, provide useful references for quantitative mineral composition studies (Green et al., 2024). These resources have substantially enriched the open data basis of the hyperspectral community, but close and traceable links among mineralogical data, geochemical data, and proximal observations are still commonly lacking.

Therefore, there remains a clear need for imaging hyperspectral datasets that focus on the same geological setting, use a consistent sensor system, systematically cover multiple proximal observation scenarios, and provide traceable mineralogical and geochemical information. Existing datasets commonly focus on a single acquisition scenario or sample type, or place greater emphasis on multi-platform remote-sensing integration. For example, the Rocklea Dome 3D Mineral Mapping Test Data Set has integrated ground-based and airborne observations (Laukamp et al., 2021), but multi-scenario proximal datasets acquired with the same sensor and centred on the same geological setting are still needed. Such datasets are particularly important for mineral mapping, hyperspectral unmixing, cross-scenario comparison, and domain-shift analysis, because they can provide a more consistent basis for comparing spectral variations across different sample forms and observation conditions while minimizing differences related to instrumentation and geological setting.

Here, we present a multi-scenario proximal SWIR hyperspectral imaging dataset that systematically covers powder, hand specimen, drill core, and in-situ outcrop observations of the same geological setting. The dataset is complemented by traceable mineralogical and geochemical information, together with corresponding metadata, processing workflows, and quality-control records. It is released as hyperspectral images and associated mineralogical and geochemical information, without further interpretative analysis, and is intended to provide a reusable basis for geological hyperspectral applications and related method development. The dataset is publicly available from Zenodo.

2 Methods and materials

2.1 Sample materials and provenance

The dataset focuses on clay-type lithium deposits as the geological setting, given their widespread occurrence and increasing resource relevance worldwide (Benson et al., 2017, 2023; Ling et al., 2021, 2024; Wen et al., 2020). Driven by the energy transition and the rapid expansion of the battery industry, demand for lithium resources continues to increase. In this context, clay-type lithium deposits are increasingly recognized as an important potential supply type in addition to salar brines and pegmatites. They have been reported and evaluated in sedimentary–volcanic basins and carbonate–clastic successions across multiple continents, indicating a broad global distribution (Meshram et al., 2014; Benson et al., 2017; Castor and Henry, 2020; Wen et al., 2020; Zhu et al., 2021; Ling et al., 2024; Ran et al., 2024). Meanwhile, these deposits commonly occur as stratified or stratiform-like lithological successions and are spatially associated with limestone, dolostone, or other sedimentary units (Liu et al., 2026; Zhang et al., 2026b). This geological setting is well suited for establishing multiscale comparisons from powder and hand specimen to drill core and in-situ outcrop, and for building a traceable observation–analysis framework. Such a framework can provide a consistent data basis for comparative studies and mineral mapping in resource exploration. Accordingly, this dataset uses clay-type lithium mineralization hosted in carbonate successions as its sample source, with most samples collected from southwest China, mainly Yunnan and Guizhou provinces. These sampling areas are mainly located within the Yangtze Block, a major Precambrian continental block in South China characterized by a crystalline basement overlain by extensive Neoproterozoic to Phanerozoic sedimentary successions, including widespread marine carbonate rocks (Cawood et al., 2018; Zhao, 2015).

From the perspectives of spectral mechanism and geological characteristics, this type of deposit is naturally suitable for imaging spectroscopy. On the one hand, clay minerals such as illite, smectite, and kaolinite, together with carbonate minerals such as calcite and dolomite, exhibit clear diagnostic absorption features in the SWIR range (Clark, 2004; Kokaly et al., 2017), which facilitates the establishment of a stable correspondence between mineral assemblages, abundance gradients, and spectral responses. On the other hand, these deposits are characterized by the coexistence of multiple minerals, spanning a continuous range from single-mineral-dominated samples to mixed-mineral assemblages. This makes them well suited for spectral unmixing, cross-scene generalization, and mineral mapping. When further combined with mineralogical and geochemical information, such as Al, K, Fe, Mg, Ca, Ti, Mn, and Sr, the dataset can provide dual constraints from both mineralogy and geochemistry. This not only improves data verifiability, but also substantially expands the transferability and comparative value of the dataset for subsequent studies.

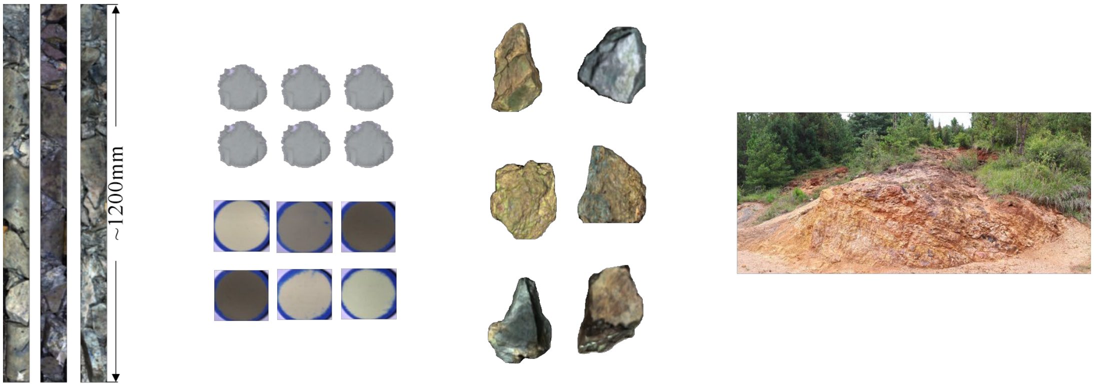

Drill cores Powder Hand specimens In-situ Outcrop

Figure 1: Representative sample types included in the dataset.

This study collected hyperspectral data for multiple sample types, covering different observation scenarios and physical forms, including drill core, corresponding powder, hand specimen, and in-situ outcrop (Figure 1). Drill core samples were scanned continuously along the core axis. Each core section was approximately 120 cm long and 10 cm in diameter. The powder was prepared from powdered materials derived from segmented drill core sampling, as well as from exploration trench and stripped outcrop sampling. Because samples from exploration trenches and stripped outcrops were mostly not standard block samples but rather loose materials, they were uniformly crushed, ground, and prepared as powder samples. Hand specimens and in-situ outcrops were both scanned repeatedly. All samples were identified using a unified coding system, and the corresponding numbering rules are provided in Table 1.

Table 1: Sample types and ID coding scheme.

Sample type	ID example	Description
Drill core	DC1111S01	Sample IDs follow the format DCxxxxSxx, where DC denotes drill core, xxxx is the drill hole ID, S indicates spectral sample, and xx is the sequence number.
Powder	PDC1111S01	Sample IDs follow the format Pxxxxxxxxx, like PDCxxxxSxx, where PDC denotes drill-core powder sample.
Exploration trench	ET1111S01	Sample IDs follow the format ETxxxxSxx, where ET denotes exploration trench, xxxx is the trench code, S indicates spectral, and xx is the sequence number.
Stripped outcrop	ST1111S01	Sample IDs follow the format STxxxxSxx, where ST denotes stripped site, xxxx is stripped outcrop ID, S indicates spectral, and xx is the sequence number.
Hand specimen	HS0001R1	Sample IDs follow the format HSxxxxRx, where HS denotes hand specimen,

		xxxx is the sample code, and Rx indicates the scan number.
In-situ outcrop	OC0001R1	Sample IDs follow the format OCxxxxRx, where OC denotes outcrop scanning, xxxx is the sample code, and Rx indicates the scan number.

2.2 HSI data acquisition and preprocessing

All proximal hyperspectral data used in this study were acquired with a HySpex Baldur S-384 N imaging spectrometer (Figure 2). The sensor operates in the shortwave infrared (SWIR) range from 960 to 2500 nm, with 384 cross-track pixels and a spectral sampling interval of 5.45 nm. Each spatial pixel records a full spectrum, resulting in 288 spectral bands (technical description available at http://hyspex.no/products/disc.php, last access: 27 March 2026). To ensure comparability across different observation scenarios, both laboratory measurements and field in-situ acquisitions were conducted using the same sensor. At the same time, differences in sample form, observation geometry, and environmental conditions were taken into account, and the acquisition strategies and subsequent processing workflows were designed separately for each observation environment.

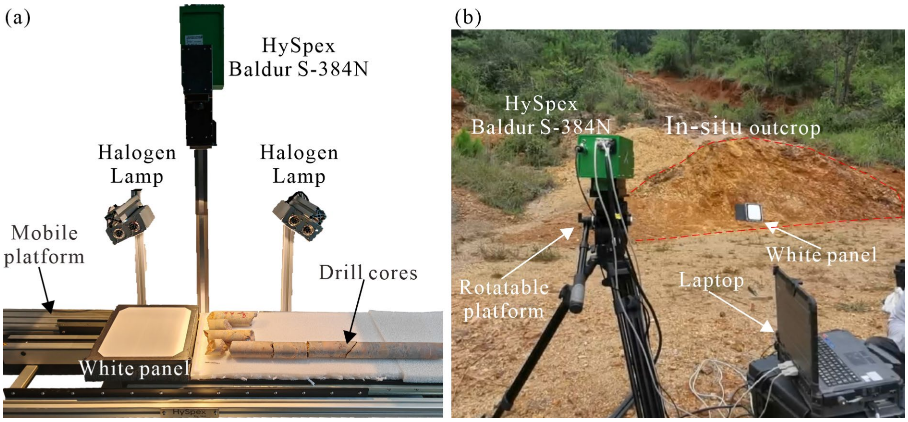

Figure 2: Instrument setup and measurement configuration. (a) laboratory scanning, (b) field in-situ scanning.

2.2.1 Laboratory HSI measurements

Except for the in-situ outcrop, all hyperspectral imaging (HSI) data were acquired indoors under controlled conditions using a moving platform for line-scan imaging (Figure 2a). During acquisition, a standard high reflectance white reference panel was used for reflectance calibration. The panel was placed at a fixed position within each image to ensure consistent calibration conditions among samples. To reduce the influence of sample height differences on imaging geometry, foam boards were used to adjust sample height so that the sample surface remained level with the white reference surface during scanning.

Laboratory measurements were conducted using two horizontally opposed halogen lamps as a stable illumination source (Figure 2a), each with a power of 360 W and an illumination angle of approximately 60°. No other light sources were present during acquisition. The sensor was equipped with a Foreoptics type 1.00 (40°) (HG) lens and operated at a working distance of approximately 0.65–0.70 m, corresponding to a field of view of about 0.27 ± 0.01 m and a spatial resolution of about 0.70 ± 0.03 mm. The maximum acquisition speed of the system was 0.30 m/s, whereas the actual scanning speed used in this study was 3.95 cm/s. The camera settings were a frame period of 18000 μs and an integration time of 2540 μs.

All HSI data were ultimately processed into reflectance format. Data acquisition was performed using HySpex Ground LAB software provided by the instrument manufacturer, and data processing was conducted using HyspexRad V3.1. The fixed white-reference correction approach was applied during preprocessing. Specifically, the start frame and end frame corresponding to the reference panel were selected as the reference region in the acquired data, and the reflectance of the white panel was set to 99.99 %. The sample data were then converted to relative reflectance based on this reference.

2.2.2 In situ HSI measurements of outcrops

In-situ outcrop hyperspectral data were acquired using the sensor mounted on a tripod platform, and line-scan imaging of the target outcrop was performed using a gimbal rotating at a constant angular velocity (Figure 2b). To reduce the effects of rapid changes in solar elevation and strong direct illumination on data quality, field acquisition was conducted under overcast conditions with relatively stable ambient light. During in-situ scanning, no foreoptic lens was installed on the sensor, and the instrument directly recorded the radiance signal from the target. The frame period was set to 18 000 μs, while other acquisition parameters were adjusted according to weather conditions and in situ irradiance levels. The scanning angular range was 60–120°, and the gimbal rotation speed was about 2.324 °/s.

Field data calibration used the same high reflectance reference panel as in the laboratory measurements. The panel was placed directly facing the sensor to ensure consistent reference observation geometry. Radiometric correction was performed using HySpexRad V3.1. Considering that field observations are affected by ambient illumination, terrain shadow, and observation geometry, the dataset provides the original radiance data together with example reflectance data derived using the empirical line method in ENVI 5.6, thereby supporting data use and comparison under different application.

2.3 Reference compositional analyses

2.3.1 Sample preparation for mineralogical and geochemical analyses

Samples used for mineralogical and geochemical analyses were further prepared from the collected materials. For stripped outcrop, exploration trench, and hand specimen samples, either the whole sample or a representative portion was selected according to sample size and integrity, and then crushed to preserve. Drill core samples were mainly collected from clay-rich intervals and their adjacent sections, so as to balance denser control of key mineral-mixing intervals with continuous coverage of the overall lithological assemblage.

Subsequent grinding and analytical sample preparation were conducted before July 2024 by ALS Laboratory Group, Guangzhou, China. The laboratory was acquired by Centre Testing International Group (CTI) in May 2025. After further crushing and grinding, all samples were reduced to a final particle size of <74 μm. One portion of the powder samples was used for geochemical analysis at ALS Laboratory, and another portion was used to mineralogical analysis and spectral measurements. The workflow of sample preparation and subsequent analyses is shown in Figure 3.

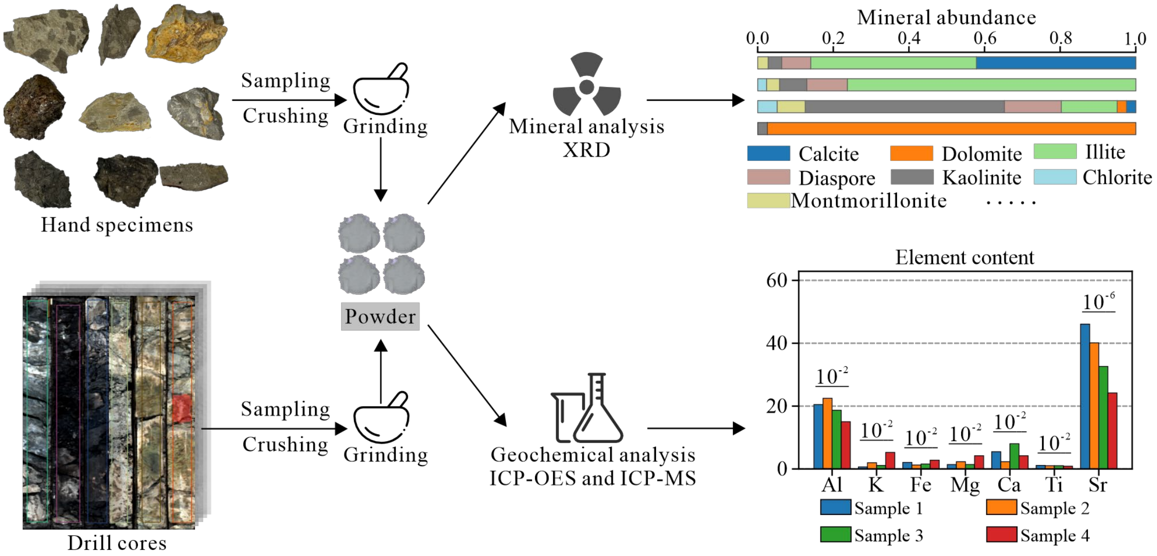

Figure 3: Workflow of powder sample preparation and subsequent mineralogical and geochemical analyses.

2.3.2 Mineralogical analyses

X-ray diffraction (XRD) has long been one of the most widely used and fundamental techniques for the identification and quantitative analysis of mineral compositions in geological samples, particularly for the recognition and comparison of crystalline phases such as clay minerals and carbonates (Chipera and Bish, 2013; Zhou et al., 2018). To obtain mineralogical information, XRD analyses were conducted on powder samples using a Shimadzu 6100Lab multifunctional X-ray diffractometer. The X-ray tube employed a Cu target operated at 40.0 kV and 30.0 mA. The slit settings were as follows: divergence slit 1.0°, scatter slit 1.0°, and receiving slit 0.300 mm. Data were collected in continuous θ–2θ scan mode over a range of 5.0–80.0° (2θ), with a scan speed of 10.0° min^{-1}, a sampling pitch of 0.0200°, and a preset time of 0.12 s. These measurement conditions were used to acquire the raw XRD diffraction patterns for subsequent quantitative analysis.

For quantitative mineralogical analysis, a QXRD workflow was applied to derive mineral phase abundances. Quantification was performed using the Full Pattern Summation (FPS) method. This approach represents the measured diffraction pattern as a combined contribution of reference diffraction patterns from individual component phases and estimates phase abundances in complex mixtures using reference intensity ratios (Butler and Hillier, 2021b; Chipera and Bish, 2013). The RockJock reference library (Eberl, 2003) was used to support the identification and quantification of mineral phases (Butler and Hillier, 2021a). The dataset provides both the raw XRD diffraction data and the mineral phase abundance results derived from the FPS analysis, allowing subsequent users to perform verification, reprocessing, and method comparison.

https://doi.org/10.5194/essd-2026-244
Preprint. Discussion started: 22 June 2026

It should be noted that the QXRD workflow adopted here represents the quantitative mineralogical approach used for this dataset, but it is not the only possible option. In addition to the FPS method based on full pattern summation, QXRD may also be performed using full-pattern fitting through Rietveld refinement (Rietveld, 1969) or by applying reference intensity ratio (RIR)-based quantification approaches (Moore and Reynolds, 1989). Different QXRD methods vary in their treatment of peak overlap, preferred orientation effects, and their dependence on reference diffraction patterns and structural models (Zhou et al., 2018). Therefore, based on the raw XRD data provided here, users may choose alternative quantification approaches according to their research objectives for further quantitative analysis and comparison.

2.3.3 Geochemical analyses

To supplement the mineralogical information and provide geochemical reference for spectral interpretation, elemental analyses were conducted on the powder samples. Considering the potential community use of the dataset, the reported elements include Al, K, Fe, Ca, Mg, Sr, Mn, and Ti. These elements characterize the major compositional variations in the clay-mineral and carbonate-mineral systems and can be linked to both spectral features and mineralogical information. Geochemical quality control information is provided in Table 2. During analysis, blank samples and certified reference materials were measured repeatedly to assess analytical stability and accuracy. Geochemical analyses were performed by ALS Laboratory Group. Samples were digested using a four-acid method involving perchloric acid, nitric acid, hydrofluoric acid, and hydrochloric acid, followed by dilution with dilute hydrochloric acid. Element concentrations were determined using ICP-OES (Agilent 5110) and ICP-MS (Agilent 7900), and the final results were obtained after correction for inter-element interferences.

Table 2: Quality control information for geochemical measurements.

Element	Al	K	Fe	Ca	Mg	Sr	Mn	Ti
Unit	%	%	%	%	%	μg/g	μg/g	%
Detection limit	0.01	0.01	0.01	0.01	0.01	0.2	5	0.005
Blank sample	<0.01	<0.01	<0.01	<0.01	<0.01	<0.2	<5	<0.005
CRM deviation (EMOG-17)	<0.06	<0.04	<0.03	<0.00	<0.00	<3.0	<15.00	<0.014
CRM deviation (MRGeo08)	<0.40	<0.15	<0.02	<0.06	<0.07	<6.00	<13.00	<0.017
CRM deviation (OREAS-45h)	<0.38	<0.01	<1.30	<0.01	<0.02	<0.60	<13.00	<0.037

Note: CRM = certified reference material.

https://doi.org/10.5194/essd-2026-244
Preprint. Discussion started: 22 June 2026

3 Results

3.1 Dataset contents and organization

This dataset comprises four scenario-specific subdatasets, including powder, drill core, hand specimen, and in-situ outcrop. The released data include hyperspectral image data, mineralogical information, geochemical information, positional and annotation information, and auxiliary files. Collectively, these data constitute a multi-scenario proximal observation dataset framework, enabling the integration of spectral observations with mineralogical and geochemical information across different types of geological materials and observation settings.

The dataset is organized according to acquisition scenario, and each subdataset contains data products specific to its sampling and measurement context (Table 3). The powder subdataset includes hyperspectral reflectance data, XRD/QXRD results, and geochemical analyses. The drill-core subdataset includes hyperspectral data, sampling annotation records, and drillhole position information. The hand-specimen subdataset contains hyperspectral reflectance data, whereas the in-situ outcrop subdataset contains hyperspectral image data and corresponding outcrop position information. The relationships among these subdatasets are established mainly through sample-based identifiers and contextual metadata. Among them, the closest correspondence exists between the drill-core and powder data, because powder was derived from selected drill-core intervals and can be associated through drillhole IDs and sampling annotation information. All data are stored in standard and widely used formats, which facilitates data access and reuse.

Table 3: Summary of released subdatasets and their organization

Subdataset	Data product	Description	Linkage key	File format
Powder	Hyperspectral data	Reflectance data	Sample ID	'.img', '.hdr'
	XRD/QXRD results	Mineralogical analysis data	Sample ID	'.csv ', '.RAW'
	Geochemical data	Geochemical analysis data	Sample ID	'.csv'
Drill core	Hyperspectral data	Reflectance data	Drillhole ID	'.img', '.hdr'
	Sampling annotation	Sampling position records	Sample ID	'.png'
	Position information	Geographic coordinates	Drillhole ID	'.csv'
Hand specimen	Hyperspectral data	Reflectance data	Sample ID	'.img', '.hdr'
In-situ outcrop	Hyperspectral data	Radiometrically corrected data	Outcrop ID	'.img', '.hdr'
	Position information	Geographic coordinates	Outcrop ID	'.csv'

3.2 Multi-scenario HSI examples

3.2.1 Powder

Hundreds of powder samples are included in the dataset. After subsampling for geochemical and mineralogical analyses, the remaining powder materials were further prepared as powder pellets for hyperspectral scanning. This preparation provided a flat and uniform surface that was suitable for measurement.

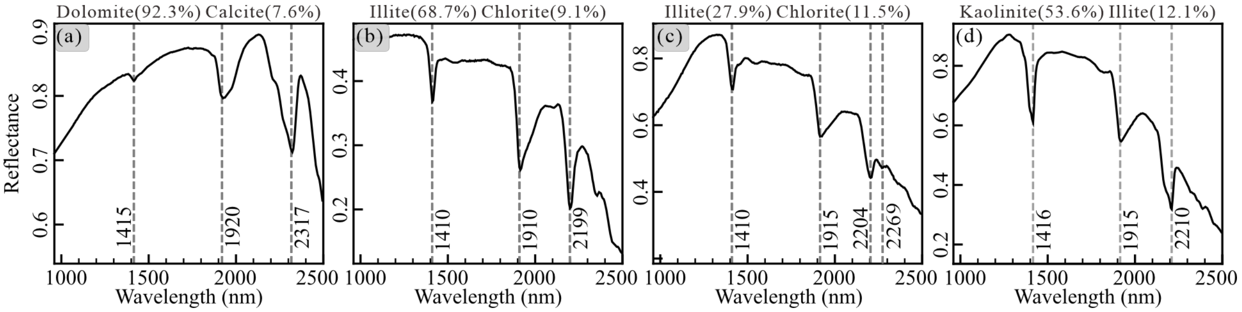

Figure 4: Representative mean reflectance spectra derived from the central 5 × 5 pixels of powder samples.

As shown in Figure 4, the powder spectra are generally smooth and display clear diagnostic mineral absorption features. Samples dominated by carbonate minerals exhibit distinct carbonate absorption features, with a diagnostic absorption near 2320 nm (Figure 4a). As the carbonate composition changes, the absorption position shifts accordingly, tending toward the longer wavelength region near 2350 nm when the calcite proportion increases. Samples dominated by illite show a pronounced absorption feature near 2200 nm (Figure 4b). With increasing mixing with other minerals, the symmetry, position, and depth of this absorption feature change markedly. When illite is mixed with chlorite, the illite related absorption shifts toward longer wavelengths, and a diagnostic chlorite absorption feature appears near 2265 nm (Figure 4c). When illite is mixed with kaolinite, a distinct left-shoulder feature develops near the 2200 nm absorption, and this feature varies with kaolinite abundance (Figure 4d).

The main mineral mixing patterns represented in the powder dataset are therefore mixtures among different clay minerals and mixtures between clay minerals and carbonate minerals. When combined with the associated mineralogical and geochemical reference data, these samples support coupled analyses of spectral features, mineral abundances, and chemical compositions.

3.2.2 Drill core

The drill core data are organized by borehole. After collection, the cores were placed in core trays for storage and hyperspectral scanning. Because the cores are mainly composed of claystone and carbonate rocks, their physical properties differ markedly. Carbonate-rich cores are generally hard and intact, whereas clay-rich cores are more fragile and tend to break after recovery. For this reason, all drill cores were scanned directly in the trays. According to tray spacing and core length, the scanned data were then rotated and cropped into individual images. As the tray width is commonly about twice the sensor swath, each tray usually required multiple scans. Like example shown in Figure 5, a tray containing 7 rows of core was scanned in three passes. The first three rows were scanned first, the fourth row was scanned after repositioning, and the remaining three rows were scanned after reversing the tray orientation. Continuous drill core images were obtained after image rotation and cropping. Because the sensor settings were unchanged, the imaging conditions and spatial resolution of the drill core data are consistent with those of the other laboratory measurements.

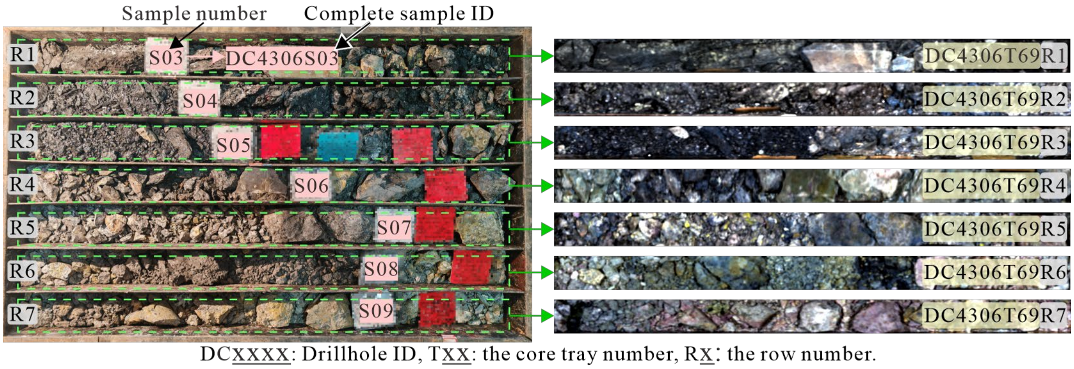

Figure 5: Example of sampling annotation, image cropping, and identifier linkage for drill core data.

Using the borehole identifiers and the corresponding sampling positions, the drill core data can be linked to the powder samples (Figure 5). Mineralogical and geochemical information obtained from powders collected from the drill cores provides reference for further interpretation of the hyperspectral data.

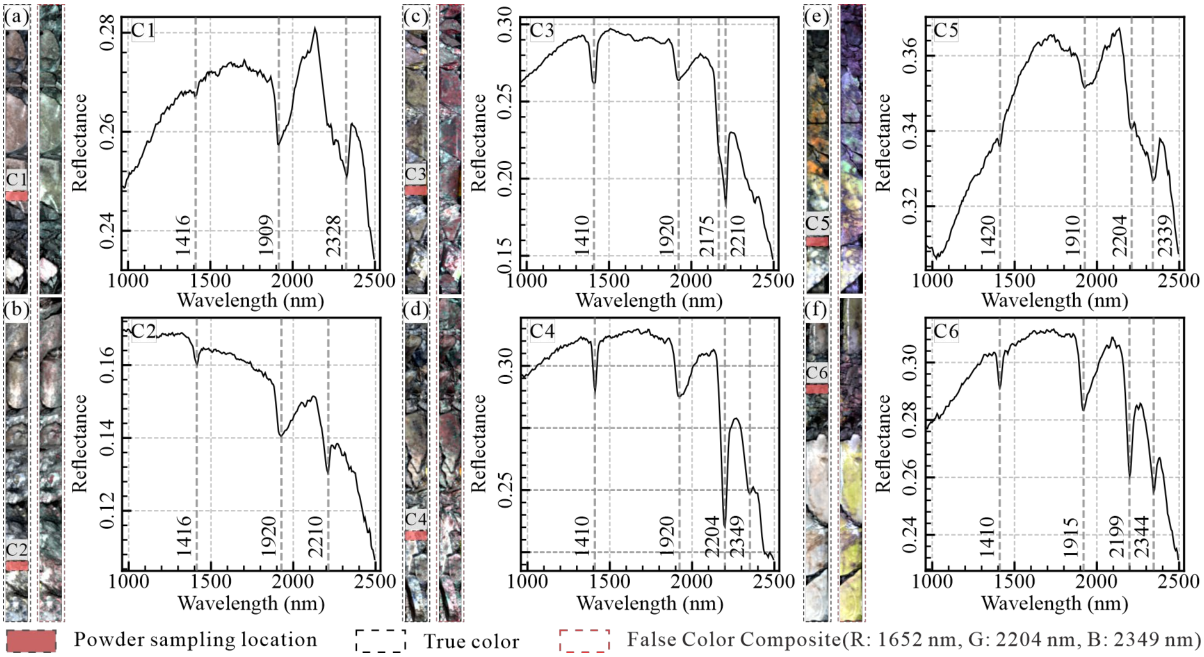

Figure 6: Representative drill core images and corresponding reflectance spectra.

The dataset provides continuous drill core images, which can reflect mineralogical variations along stratigraphic depth. As shown in Figure 6, panels a to f illustrate representative transitions from dolostone to claystone and then to limestone, together with their sample characteristics and lithological transition features. Carbonate-dominated intervals, such as those in Figure 6a and f, their spectra display clear diagnostic carbonate absorption features near 2350 nm. In transitional intervals between claystone and carbonate, the spectra show clear signatures of intimate mixing between clay minerals and carbonate minerals, with pronounced absorptions near 2200 and 2350 nm (Figure 6f). Clay-rich intervals appear red in the false-colour images because of the strong absorption near 2200 nm (Figure 6c and d). Mixing among clay minerals can further change both the absorption position and the absorption shape, which is consistent with the patterns observed in the powder samples.

3.2.3 Hand specimen

The hand-specimen data were acquired using the laboratory sensor configuration, measurement environment and parameters as the powder and drill core. They therefore form part of the same multi-scenario proximal SWIR data framework. Lithologically, these samples include limestone, dolostone, and claystone. Structurally, they cover compact massive, clastic, and oolitic types, thereby reflecting the diversity of mineral composition and textural organization on natural geological surfaces. Unlike the relatively uniform surfaces of powder samples, hand specimens commonly show pronounced spatial heterogeneity. Local differences in grain composition and texture are often associated with distinct spectral responses.

As shown in Figure 7, the hyperspectral images and reflectance spectra extracted from corresponding locations directly illustrate spectral variations within individual samples. Even in visually dense and relatively homogeneous specimens, different locations may still exhibit clear differences in mineral absorption features. This indicates that the hand-specimen data effectively capture the component and surface heterogeneity present in natural samples.

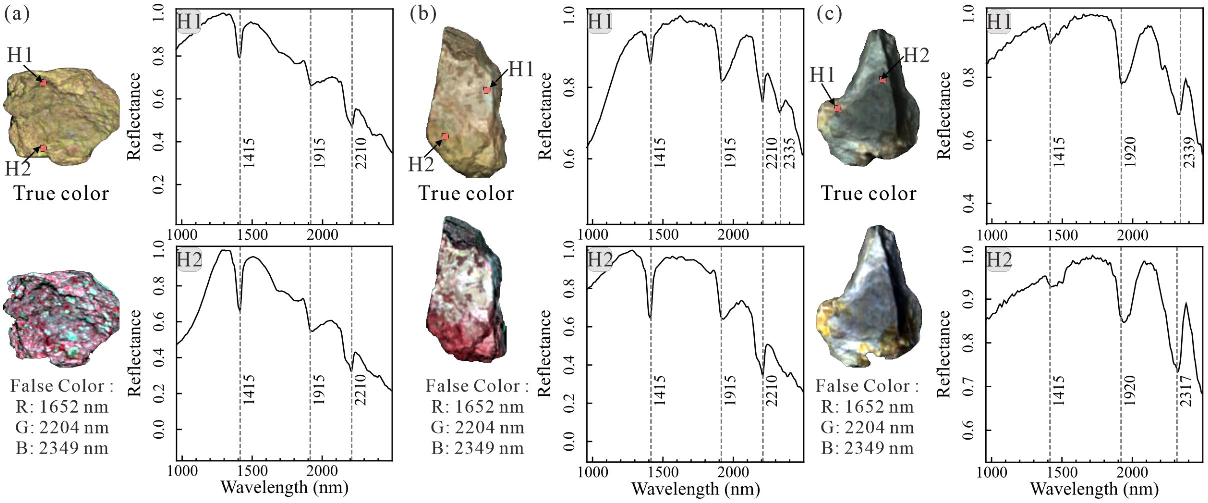

Figure 7: Representative hand specimen images and corresponding reflectance spectra.

3.2.4 In situ outcrop

The in-situ outcrop data were acquired using the same sensor and the same geological setting as in the other scenarios, ensuring comparability across the dataset. Because outcrop measurements were collected in an uncontrolled field environment, they are more strongly affected by variations in solar illumination, observation geometry, and atmospheric water vapour. For this reason, the dataset primarily provides radiometrically corrected imagery, while reflectance data are not treated as the only formal data product.

Figure 8 presents an example of reflectance retrieval using the empirical line method in ENVI 5.6. The spectra of representative points S1 to S3 show that clear diagnostic absorption features can still be identified within the main usable wavelength range, including the left-shoulder feature of kaolinite near 2200 nm, the illite-related absorption near 2200 nm, and the chlorite-related absorption near 2265 nm. This indicates that, after appropriate correction, the in-situ outcrop data can support mineral identification and related spectral analysis. Point S4 shows the reflectance spectrum of the reference panel after correction. Except for the strong atmospheric water-vapour absorption regions, its reflectance remains close to 100% across other wavelengths, suggesting that the method can provide generally reasonable reflectance recovery within the main usable bands.

It should also be noted that the quality of the in-situ outcrop data is strongly constrained by field conditions. In particular, the atmospheric water-vapour absorption regions near 1400 and 1900 nm usually show relatively low signal-to-noise ratios and poor spectral stability, and are therefore generally not recommended for direct mineral identification or quantitative analysis. In addition, the empirical-line reflectance results may be influenced by selection of the region of interest and other operational factors. To reduce these effects as far as possible, each outcrop was scanned multiple times, and the sensor was positioned to maintain a near-normal view of the reference panel during acquisition. To preserve data traceability and methodological flexibility, the dataset therefore gives priority to the release of radiometrically corrected data and reference panel spectra, and users are encouraged to select their own reflectance correction workflow and wavelength range according to specific research objectives.

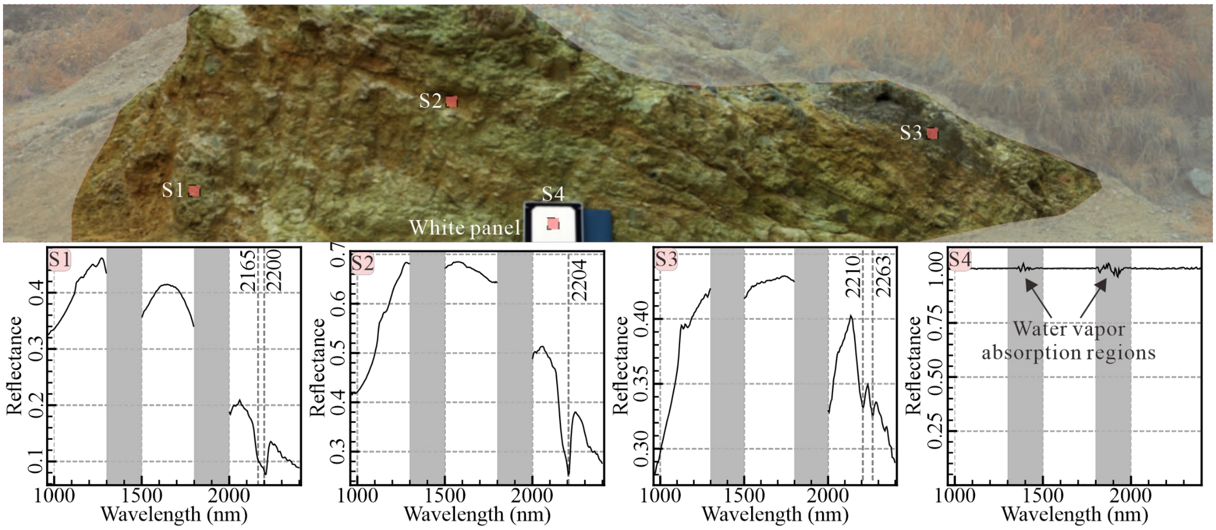

Figure 8: **Representative in situ outcrop images and corresponding reflectance spectra [4x4 AVG].**

3.3 Mineralogical and geochemical reference

In addition to the hyperspectral data, the dataset also provides sample-linked reference mineralogical and geochemical information to enhance data interpretability and reusability. The geochemical data include elemental results together with the corresponding quality control files, allowing users to assess analytical reliability, trace the testing process, and perform further screening and use according to specific research needs. These reference data can serve not only as supporting information for the interpretation and validation of the hyperspectral data, but also as a basis for coupled analyses of mineral composition, elemental characteristics, and spectral responses.

For the mineralogical information, both the raw XRD data and the mineral abundance results derived from the QXRD are provided. To improve data transparency and reusability, the dataset retains the raw diffraction patterns and also includes the mineral phase interpretations and quantitative results adopted in this study, together with reference merging schemes for phases subdivided by crystal type or structural state. For example, where phases belong to the same mineral group but differ in crystal structure, degree of structural ordering, or naming level, corresponding grouping suggestions are provided. This allows users to select a mineral class representation more appropriate for mineral mapping, statistical analysis, or model training according to their research objectives. These schemes are intended as references rather than fixed standards. Because the raw XRD data, QXRD results, and related metadata are all fully provided, users may still reclassify, merge, or reprocess the mineral phases according to their own needs. Figure 9 presents the measured XRD patterns and QXRD fitted results for two representative samples, including a claystone sample and a carbonate rock sample.

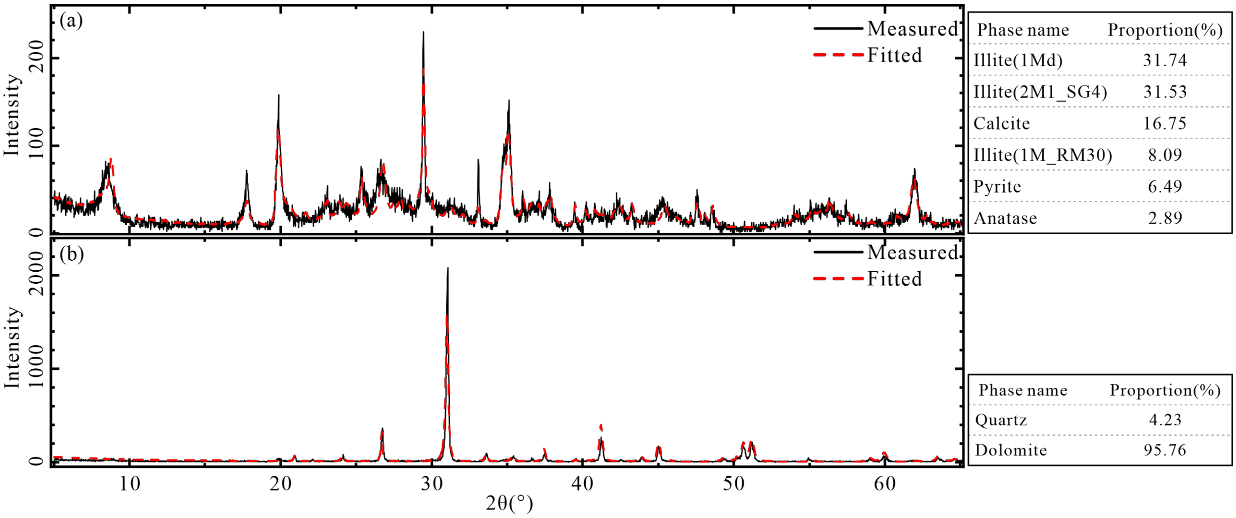

Phase name	Proportion(%)
Illite(1Md)	31.74
Illite(2M1_SG4)	31.53
Calcite	16.75
Illite(1M_RM30)	8.09
Pyrite	6.49
Anatase	2.89

Phase name	Proportion(%)
Quartz	4.23
Dolomite	95.76

Figure 9: Comparison between measured XRD patterns and QXRD fitted profiles for representative samples. (a) an illite-rich claystone, (b) a carbonate rock.

The value of these mineralogical and geochemical data lies not only in providing independent reference information for the hyperspectral observations, but also in their potential coupling with the hyperspectral data. For the clay and carbonate mineral systems represented in this work, characteristic SWIR absorptions are commonly related to cation–hydroxyl associations, crystal-chemical properties, and mineral abundance variations, which in turn often correspond to changes in elemental concentrations. Mineral abundances, elemental concentrations, and hyperspectral absorption features may therefore contain exploitable associations and potentially quantitative relationships. Figure 10 shows the relationships between mineral abundances and elemental contents, including the correlations of carbonate minerals with Ca and Mg, illite with K, and kaolinite with Al. These patterns indicate that the mineralogical and geochemical information is highly complementary and highlight the potential of the dataset for mineral–element–spectral coupling analysis, feature interpretation, and related modelling studies.

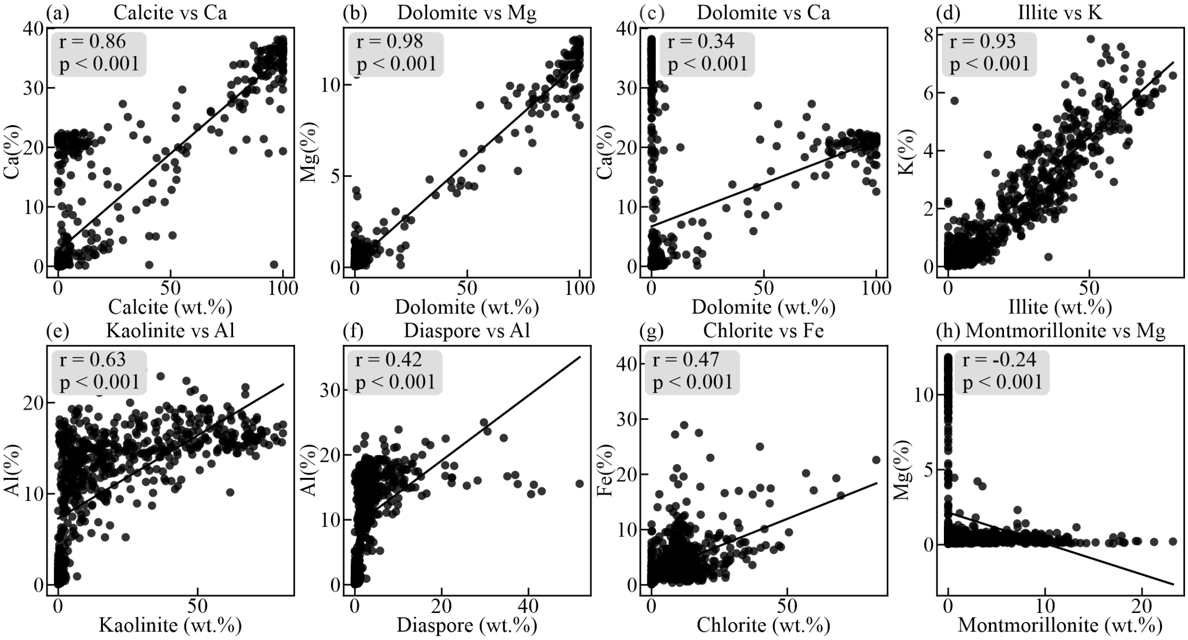

Figure 10: Relationships between mineral abundances and corresponding elemental concentrations.

4 Discussion

The value of the dataset lies not only in its multi-scenario observations, but also in its response to the need within the geological hyperspectral community for publicly available data resources with mineralogical and geochemical reference information. Hyperspectral data have been widely used for lithological identification, mineral mapping, and mineral exploration, but spectral interpretation, model calibration, and result validation commonly require independent mineralogical and geochemical constraints (Cavalli, 2023; Koerting et al., 2021; Peyghambari and Zhang, 2021; Van Der Meer et al., 2012). The development of such open reference datasets has therefore continued to be recognized as an important foundation for geological hyperspectral research. Within a unified framework, this dataset systematically covers four complementary proximal SWIR observation scenarios, including powder, drill core, hand specimen, and in-situ outcrop, and further integrates XRD/QXRD and geochemical reference. In this way, it links spectral observations with mineralogical and geochemical analyses, thereby providing a basis for the interpretation and validation of future studies.

Compared with existing geological hyperspectral open data resources, the contribution of this dataset does not lie in providing a broader general spectral library or a larger geological hyperspectral database. Instead, it lies in establishing a multi-scenario data framework centred on the same geological setting, acquired with the same sensor, and linked across scenarios in a traceable manner. Existing resources such as RELAB (Milliken, 2019), the USGS Spectral Library (Kokaly et al., 2017), and GREENPEG (Cardoso-Fernandes et al., 2023) are primarily designed as broad reference spectral libraries for laboratory, field, or specific material types, and provide essential support for material identification and spectral comparison.

However, these libraries are commonly based on point spectrometer measurements. Imaging datasets such as HIDSAG and NVCL are closer to the present dataset in terms of imaging format, but their samples are generally treated as independent scanning objects, with emphasis on providing high quality training and test data rather than building a cross-scenario, traceable observation chain around the same geological setting (Ehrenfeld et al., 2023; Huntington, 2016). The Rocklea Dome 3D Mineral Mapping Test Data Set places greater emphasis on the integration of multi-platform observations and mine-scale 3D mineral mapping (Laukamp et al., 2021). In contrast, the present dataset is more specifically focused on a proximal, sample-scale, multi-scenario imaging chain and is further supported by traceable mineralogical and geochemical reference information, thereby providing a useful data basis for related applications.

Accordingly, this dataset can support not only mineral mapping and feature interpretation, but also the validation of hyperspectral unmixing and quantitative mineral analysis under real sample conditions. At the same time, the consistency of the geological setting and sensor system makes the dataset suitable for cross-scenario generalization and domain adaptation studies. In addition, this is not a small demonstration dataset, its scale and data quality are sufficient to support the training and validation of supervised and unsupervised machine learning and deep learning methods. Overall, the dataset can serve not only geological analysis and interpretation, but also the testing and validation of deep learning, transfer learning, and spectral unmixing models, as well as studies linking proximal observations with mineral mapping at broader scales.

It should be noted that, although this dataset establishes links between multi-scenario proximal observations and reference information, inherent differences remain in acquisition geometry, surface condition, and environmental setting among the different scenarios. The data from different scenarios should therefore not be treated as equivalent observations acquired under fully identical conditions (Ruitenbeek et al., 2025). In addition, although the mineralogical and geochemical information provides reference within the dataset, it represents the analytical scale after sampling and sample preparation and should not be regarded as a pixel-scale ground truth at the sampling location. Natural samples are commonly heterogeneous, and the powders used for analyses are generally collected from a short core interval or a limited local area to obtain sufficient material. These data are therefore more appropriately used as reference information or constraints.

5 Data availability

The dataset described in this manuscript can be accessed at https://doi.org/10.5281/zenodo.19142250 (Zhang et al., 2026a). These hyperspectral data can be read using open-source tools such as EnMAP-Box (https://enmap-box.readthedocs.io), Spectral Python (https://www.spectralpython.net), and Rasterio (https://rasterio.readthedocs.io).

6 Conclusions and outlook

This study provides a multi-scenario proximal SWIR imaging hyperspectral dataset covering powder, drill core, hand specimen, and in-situ outcrop, together with associated mineralogical and geochemical reference information. Its main value lies in establishing a multi-scenario and internally linked reference framework that couples hyperspectral observations with mineralogical and geochemical constraints across complementary geological sample forms and observation settings. As a substantial, traceable multi-scenario proximal observation dataset, it provides a data basis for training, validation, and coupling analysis in mineral mapping, spectral feature interpretation, cross-scenario generalization, and related model development. Moreover, the dataset is accompanied by metadata, quality-control files, and usage examples, while the raw data and reference information are retained to support further user-defined processing and reuse. In the future, the dataset may also be used together with other relevant datasets and support the connection between proximal observations and airborne or spaceborne hyperspectral observations.

Author contributions

LL conceptualized and developed the methodology of this paper. QZ and JM curated the data. QZ conducted formal analysis, visualizations and wrote the original draft. QZ and LL contributed to writing, reviewing and editing the manuscript.

Competing interests

The authors declare that they have no conflict of interest.

Financial support

This work was supported by the National Key Research and Development Program of China (grant nu. 2024YFC2909905).

References

Baldridge, A. M., Hook, S. J., Grove, C. I., and Rivera, G.: The ASTER spectral library version 2.0, Remote Sens. Environ., 113, 711–715, https://doi.org/10.1016/j.rse.2008.11.007, 2009.

Benson, T. R., Coble, M. A., Rytuba, J. J., and Mahood, G. A.: Lithium enrichment in intracontinental rhyolite magmas leads to Li deposits in caldera basins, Nat. Commun., 8, 270, https://doi.org/10.1038/s41467-017-00234-y, 2017.

Benson, T. R., Coble, M. A., and Dilles, J. H.: Hydrothermal enrichment of lithium in intracaldera illite-bearing claystones, Sci. Adv., 9, eadh8183, https://doi.org/10.1126/sciadv.adh8183, 2023.

Booysen, R., Lorenz, S., Thiele, S. T., Fuchsloch, W. C., Marais, T., Nex, P. A. M., and Gloaguen, R.: Accurate hyperspectral imaging of mineralised outcrops: An example from lithium-bearing pegmatites at Uis, Namibia, Remote Sens. Environ., 269, 112790, https://doi.org/10.1016/j.rse.2021.112790, 2022.

Borsoi, R. A., Imbiriba, T., Bermudez, J. C. M., Richard, C., Chanussot, J., Drumetz, L., Tourneret, J.-Y., Zare, A., and Jutten, C.: Spectral Variability in Hyperspectral Data Unmixing: A comprehensive review, IEEE Geosci. Remote Sens. Mag., 9, 223–270, https://doi.org/10.1109/MGRS.2021.3071158, 2021.

Butler, B. M. and Hillier, S.: Automated full-pattern summation of X-ray powder diffraction data for high-throughput quantification of clay-bearing mixtures, Clays Clay Miner., 69, 38–51, https://doi.org/10.1007/s42860-020-00105-6, 2021a.

Butler, B. M. and Hillier, S.: powdR: An R package for quantitative mineralogy using full pattern summation of X-ray powder diffraction data, Comput. Geosci., 147, 104662, https://doi.org/10.1016/j.cageo.2020.104662, 2021b.

Cardoso-Fernandes, J., Santos, D., Rodrigues de Almeida, C., Lima, A., Teodoro, A. C., and GREENPEG project team: Spectral Library of European Pegmatites, Pegmatite Minerals and Pegmatite Host-Rocks – the GREENPEG project database, Earth Syst. Sci. Data, 15, 3111–3129, https://doi.org/10.5194/essd-15-3111-2023, 2023.

Castor, S. B. and Henry, C. D.: Lithium-Rich Claystone in the McDermitt Caldera, Nevada, USA: Geologic, Mineralogical, and Geochemical Characteristics and Possible Origin, Minerals, 10, 68, https://doi.org/10.3390/min10010068, 2020.

Cavalli, R. M.: Spatial Validation of Spectral Unmixing Results: A Systematic Review, Remote Sens., 15, 2822, https://doi.org/10.3390/rs15112822, 2023.

Cawood, P. A., Zhao, G., Yao, J., Wang, W., Xu, Y., and Wang, Y.: Reconstructing South China in Phanerozoic and Precambrian supercontinents, Earth-Sci. Rev., 186, 173–194, https://doi.org/10.1016/j.earscirev.2017.06.001, 2018.

Chipera, S. J. and Bish, D. L.: Fitting Full X-Ray Diffraction Patterns for Quantitative Analysis: A Method for Readily Quantifying Crystalline and Disordered Phases, Advances in Materials Physics and Chemistry, 3, 47–53, https://doi.org/10.4236/ampc.2013.31A007, 2013.

Clark, R. N.: Spectroscopy of rocks and minerals, and principles of spectroscopy, in: Infrared Spectroscopy in Geochemistry, Exploration Geochemistry and Remote Sensing, Mineralogical Association of Canada, 17–55, 2004.

Clark, R. N., Swayze, G. A., Livo, K. E., Kokaly, R. F., Sutley, S. J., Dalton, J. B., McDougal, R. R., and Gent, C. A.: Imaging spectroscopy: Earth and planetary remote sensing with the USGS Tetracorder and expert systems, J. Geophys. Res. Planets, 108, https://doi.org/10.1029/2002JE001847, 2003.

Clark, R. N., Swayze, G. A., Wise, R. A., Livo, K. E., Hoefen, T. M., Kokaly, R. F., and Sutley, S. J.: USGS digital spectral library splib06a, US Geological Survey, https://doi.org/10.3133/ds231, 2007.

Corrado, F., Putzolu, F., Armstrong, R. N., Mondillo, N., Chirico, R., Casarotto, B., Massironi, M., Fuller, D., Ball, R., and Herrington, R. J.: Application of satellite and proximal hyperspectral sensing to target lithium mineralization in volcano-sedimentary deposits: A case study from the McDermitt caldera, USA, Remote Sens. Environ., 323, 114724, https://doi.org/10.1016/j.rse.2025.114724, 2025.

Eberl, D. D.: User Guide to RockJock - A Program for Determining Quantitative Mineralogy from X-Ray Diffraction Data, Open-File Report, U.S. Geological Survey, https://doi.org/10.3133/ofr200378, 2003.

Ehrenfeld, A., Egaña, Á. F., Santibañez-Leal, F., Garrido, F., Ojeda, M., Townley, B., and Navarro, F.: HIDSAG: Hyperspectral Image Database for Supervised Analysis in Geometallurgy, Sci. Data, 10, 164, https://doi.org/10.1038/s41597-023-02061-x, 2023.

Goetz, A. F. H., Vane, G., Solomon, J. E., and Rock, B. N.: Imaging Spectrometry for Earth Remote Sensing, Science, 228, 1147–1153, https://doi.org/10.1126/science.228.4704.1147, 1985.

Green, C. J., Alfaro, O. E., Taylor, K. A., Singh, K., Hoppe, D. A., Piatak, N., and Seal, R. R.: X-ray diffraction data and estimates of mineral abundances based on Rietveld refinement for mine wastes collected through the USGS Earth Mapping Resources Initiative (ver. 2.0, April 2025), https://doi.org/10.5066/P1O732BG, 2024.

Hajaj, S., El Harti, A., Pour, A. B., Jellouli, A., Adiri, Z., and Hashim, M.: A review on hyperspectral imagery application for lithological mapping and mineral prospecting: Machine learning techniques and future prospects, Remote Sens. Appl.: Soc. Environ., 35, 101218, https://doi.org/10.1016/j.rsase.2024.101218, 2024.

Hunt, G. R.: Spectral signatures of particulate minerals in the visible and near infrared, Geophysics, 42, 501–513, https://doi.org/10.1190/1.1440721, 1977.

Huntington, J.: Uncovering the mineralogy of the Australian Continent: the AuScope National Virtual Core Library. A national hyperspectrally derived drill-core archive, Aust. J. Earth Sci., 63, 923–928, https://doi.org/10.1080/08120099.2016.1269630, 2016.

Koerting, F., Koellner, N., Kuras, A., Boesche, N. K., Rogass, C., Mielke, C., Elger, K., and Altenberger, U.: A solar optical hyperspectral library of rare-earth-bearing minerals, rare-earth oxide powders, copper-bearing minerals and Apliki mine surface samples, Earth Syst. Sci. Data, 13, 923–942, https://doi.org/10.5194/essd-13-923-2021, 2021.

Kokaly, R. F., Clark, R. N., Swayze, G. A., Livo, K. E., Hoefen, T. M., Pearson, N. C., Wise, R. A., Benzel, W., Lowers, H. A., and Driscoll, R. L.: USGS spectral library version 7, US Geological Survey, https://doi.org/10.3133/ds1035, 2017.

Laukamp, C., Haest, M., and Cudahy, T.: The Rocklea Dome 3D Mineral Mapping Test Data Set, Earth Syst. Sci. Data, 13, 1371–1383, https://doi.org/10.5194/essd-13-1371-2021, 2021.

Ling, K., Wen, H., Zhang, Q., Luo, C., Gu, H., Du, S., and Yu, W.: Super-enrichment of lithium and niobium in the upper Permian Heshan Formation in Pingguo, Guangxi, China, Sci. China Earth Sci., 64, 753–772, https://doi.org/10.1007/s11430-020-9752-6, 2021.

Ling, K., Wen, H., Han, T., Lu, Z., Cui, Y., Luo, C., and Yu, W.: Lithium-rich claystone in Pingguo area, Guangxi, southwest China: precursor kaolinite controls lithium enrichment, Miner. Depos., 59, 329–340, https://doi.org/10.1007/s00126-023-01210-x, 2024.

Liu, L., Yin, C., Wen, H., and Zhang, G.: Mapping lithium hosting claystone using WorldView-3 image and deep learning method, Gondwana Res., 151, 18–35, https://doi.org/10.1016/j.gr.2025.10.012, 2026.

Lorenz, S., Ghamisi, P., Kirsch, M., Jackisch, R., Rasti, B., and Gloaguen, R.: Feature extraction for hyperspectral mineral domain mapping: A test of conventional and innovative methods, Remote Sens. Environ., 252, 112129, https://doi.org/10.1016/j.rse.2020.112129, 2021.

Meerdink, S. K., Hook, S. J., Roberts, D. A., and Abbott, E. A.: The ECOSTRESS spectral library version 1.0, Remote Sens. Environ., 230, 111196, https://doi.org/10.1016/j.rse.2019.05.015, 2019.

Meshram, P., Pandey, B. D., and Mankhand, T. R.: Extraction of lithium from primary and secondary sources by pre-treatment, leaching and separation: A comprehensive review, Hydrometallurgy, 150, 192–208, https://doi.org/10.1016/j.hydromet.2014.10.012, 2014.

Milliken, R.: RELAB spectral library bundle, NASA Planetary Data System, 117, https://doi.org/10.17189/1519032, 2019.

Moore, D. M. and Reynolds, R. C.: X-ray Diffraction and the Identification and Analysis of Clay Minerals., Oxford University Press, Oxford, 1989.

Peyghambari, S. and Zhang, Y.: Hyperspectral remote sensing in lithological mapping, mineral exploration, and environmental geology: An updated review, J. Appl. Remote Sens., 15, https://doi.org/10.1117/1.JRS.15.031501, 2021.

Ran, Y., Qu, G., Yang, J., Zhou, S., Li, B., Wang, H., and Wei, Y.: Efficient separation and extraction of lithium from low-grade claystone by chloride salt-enhanced roasting process, J. Clean. Prod., 434, 140156, https://doi.org/10.1016/j.jclepro.2023.140156, 2024.

Rasti, B., Zouaoui, A., Mairal, J., and Chanussot, J.: Image Processing and Machine Learning for Hyperspectral Unmixing: An Overview and the HySUPP Python Package, IEEE Trans. Geosci. Remote Sens., 62, 1–31, https://doi.org/10.1109/TGRS.2024.3393570, 2024.

Rietveld, H. M.: A profile refinement method for nuclear and magnetic structures, J. Appl. Crystallogr., 2, 65–71, https://doi.org/10.1107/S0021889869006558, 1969.

Ruitenbeek, F. J. A. van, Bakker, W. H., Werff, H. M. A. van der, Hecker, C. A., Hein, K. A. A., and Eijndthoven, W. van: A Knowledge-Based Strategy for Interpretation of SWIR Hyperspectral Images of Rocks, Remote Sens., 17, 2555, https://doi.org/10.3390/rs17152555, 2025.

Scafutto, R. D. M., Souza Filho, C. R. de, and Rivard, B.: Characterization of mineral substrates impregnated with crude oils using proximal infrared hyperspectral imaging, Remote Sens. Environ., 179, 116–130, https://doi.org/10.1016/j.rse.2016.03.033, 2016.

Schodlok, M. C., Whitbourn, L., Huntington, J., Mason, P., Green, A., Berman, M., Coward, D., Connor, P., Wright, W., Jolivet, M., and Martinez, R.: HyLogger-3, a visible to shortwave and thermal infrared reflectance spectrometer system for drill core logging: functional description, Aust. J. Earth Sci., 63, 929–940, https://doi.org/10.1080/08120099.2016.1231133, 2016.

Swayze, G. A., Clark, R. N., Goetz, A. F. H., Livo, K. E., Breit, G. N., Kruse, F. A., Sutley, S. J., Snee, L. W., Lowers, H. A., Post, J. L., Stoffregen, R. E., and Ashley, R. P.: Mapping Advanced Argillic Alteration at Cuprite, Nevada, Using Imaging Spectroscopy, Econ. Geol., 109, 1179–1221, https://doi.org/10.2113/econgeo.109.5.1179, 2014.

Van Der Meer, F. D., Van Der Werff, H. M. A., Van Ruitenbeek, F. J. A., Hecker, C. A., Bakker, W. H., Noomen, M. F., Van Der Meijde, M., Carranza, E. J. M., Smeth, J. B. D., and Woldai, T.: Multi- and hyperspectral geologic remote sensing: A review, Int. J. Appl. Earth Obs. Geoinf., 14, 112–128, https://doi.org/10.1016/j.jag.2011.08.002, 2012.

Wen, H., Luo, C., Du, S., Yu, W., Gu, H., Ling, K., Cui, Y., Li, Y., and Yang, J.: Carbonate-hosted clay-type lithium deposit and its prospecting significance, Chin. Sci. Bull., 65, 53–59, https://doi.org/10.1360/TB-2019-0179, 2020.

Windrim, L., Melkumyan, A., Murphy, R. J., Chlingaryan, A., and Leung, R.: Unsupervised ore/waste classification on open-cut mine faces using close-range hyperspectral data, Geosci. Front., 14, 101562, https://doi.org/10.1016/j.gsf.2023.101562, 2023.

Zhang, Q., Liu, L., and Mei, J.: Proximal Multi-Scenario SWIR Hyperspectral Mineral Abundance Dataset, Zenodo [Data set], https://doi.org/10.5281/zenodo.19142250, 2026a.

Zhang, Q., Mei, J., Lin, L., Liu, L., Wen, H., and Wang, L.: Sorting carbonate clay-type lithium ores using a deep learning model with adaptive spectral-texture feature fusion, Geosci. Front., 17, 102185, https://doi.org/10.1016/j.gsf.2025.102185, 2026b.

Zhao, G.: Jiangnan Orogen in South China: Developing from divergent double subduction, Gondwana Res., 27, 1173–1180, https://doi.org/10.1016/j.gr.2014.09.004, 2015.

Zhou, X., Liu, D., Bu, H., Deng, L., Liu, H., Yuan, P., Du, P., and Song, H.: XRD-based quantitative analysis of clay minerals using reference intensity ratios, mineral intensity factors, Rietveld, and full pattern summation methods: A critical review, Solid Earth Sci., 3, 16–29, https://doi.org/10.1016/j.sesci.2017.12.002, 2018.

Zhu, L., Gu, H., Wen, H., and Yang, Y.: Lithium extraction from clay-type lithium resource using ferric sulfate solutions via an ion-exchange leaching process, Hydrometallurgy, 206, 105759, https://doi.org/10.1016/j.hydromet.2021.105759, 2021.

Zou, J., Qu, H., and Zhang, P.: Conventional to Deep Learning Methods for Hyperspectral Unmixing: A Review, Remote Sens., 17, 2968, https://doi.org/10.3390/rs17172968, 2025.